Correlating structural disorder to Li⁺ ion transport in $\text{Li}_{4-x}\text{Ge}_{1-x}\text{Sb}_x\text{S}_4$ ($0 \le x \le 0.2$)

Bianca Helm,^a Nicolò Minafra,^a Björn Wankmiller,^{a,b,c} Matthias T. Agne,^d Cheng Li,^e Anatoliy Senyshyn,^f Michael Ryan Hansen,^c and Wolfgang G. Zeier*^{a,d}

^aInstitute of Inorganic and Analytical Chemistry, University of Münster, Corrensstrasse 28/30, D-48149 Münster, Germany.

^bInternational Graduate School for Battery Chemistry, Characterization, Analysis, Recycling and Application (BACCARA), University of Münster, Corrensstrasse 40, D-48149 Münster, Germany

^cInstitute of Physical Chemistry, University of Münster, Corrensstrasse 30, D-48149 Münster, Germany.

^dInstitut für Energie- und Klimaforschung (IEK), IEK-12: Helmholtz-Institut Münster, Forschungszentrum Jülich, 48149 Münster, Germany.

^eNeutron Scattering Division, Oak Ridge National Laboratory (ORNL), 1 Bethel Valley Road, Oak Ridge, Tennessee 37831-6473, United States.

^fHeinz Maier-Leibnitz Zentrum, Technical University of Munich, D-85748 Garching, Germany

*wzeier@uni-muenster.de

Abstract

Strong compositional influences are known to affect the ionic transport within the thio-LISICON family, however, a deeper understanding of the resulting structure - transport correlations have up until now been lacking. Employing a combination of high-resolution neutron diffraction, impedance spectroscopy and nuclear magnetic resonance spectroscopy, together with bond valence site energy calculations and the maximum entropy method for determining the underlying Li⁺ scattering density distribution of a crystal structure, this work assesses the impact of the Li⁺ substructure and charge carrier density on the ionic transport within the Li_{4-x}Ge_{1-x}Sb_xS₄ substitution series. By incorporating Sb⁵⁺ into Li₄GeS₄, an anisometric expansion of the unit cell is observed. An additional Li⁺ position is found as soon as (SbS₄)³⁻ polyhedra are present, leading to a better local polyhedral connectivity and a higher disorder in the Li⁺ substructure. Here, we are able to relate structural disorder to an increase in configurational entropy, together with a two order-of-magnitude increase in ionic conductivity. This result reinforces the typically believed paradigm that structural disorder leads to improvements in ionic transport.

1. Introduction

The aim to enhance the safety of current state-of-the-art lithium-ion batteries involves the replacement of the liquid electrolyte with a solid electrolyte.^{1–3} However, for the successful application in solid-state batteries, solid ionic conductors need to achieve high ionic conductivities at least as high as their liquid counterparts.^{2,3} The ionic conductivities in crystalline solid electrolytes can be tuned by finding a beneficial polyhedral connectivity,⁴ tailoring the width of diffusion pathways,^{5–7} tuning the lattice polarizability,^{6,8,9} and changing the carrier density.^{7,10–12} In addition, for solid-state battery performance a mechanical softness of the solid electrolytes is desired for simplifying manufacturing.¹³ Thus, the transition from purely oxide-based solid electrolytes, which are mechanically hard, to sulfide-^{9,14,15} and recently halide-based materials^{16–18} was predictable, as they are mechanically soft and cold pressing is suitable for densification.¹³ As examples, sulfide-based solid electrolyte materials classes include the argyrodites,^{9,19–21} Li₁₀GeP₂S₁₂,^{15,22–25} and thio-LISICONs (LIthium SuperIonic CONductor).^{10,26,27} The latter material class was developed from their oxide-based counterpart the LISICONs, where the exchange of the anion from the less polarizable oxygen to the more polarizable sulfur has improved the ionic conductivity significantly.¹⁴

The thio-LISICON Li₄GeS₄ crystallizes in the orthorhombic space group *Pnma* (Figure 1). ^{26,28,29} The sulfur atoms form a distorted hexagonal close-packing (Figure 1a) and the structure consists of (GeS₄)⁴⁻ tetrahedra, two tetrahedrally coordinated Li(1) and Li(2) positions in addition to an octahedrally coordinated Li(3) lithium position (Figure 1e).

The Li₄GeS₄ structure is mainly composed of lithium polyhedra, while the anionic framework is built of isolated (GeS₄)⁴⁻ tetrahedra arranged with alternating apices similar to the β -Li₃PS₄ structure (Figure 1b). The Li(3) octahedra are edge-sharing and form a chain along the *b*-axis which is the main diffusion pathway for Li₄GeS₄ (Figure 1c).^{5,27,30} Li(1) is corner- and edge-sharing to Li(3) and bridges two Li(3) octahedra (Figure 1d). The other tetrahedral position Li(2) shares faces and corners with Li(3). The Li(2) tetrahedra share corners with each other (Figure 1e). This work identifies lithium ions on an additional crystallographic site Li(4) in the Li₄GeS₄ structure (Figure 1f). A similar Li⁺ substructure was recently observed in Li₄GeSe₄ reported by Minafra *et al*.²⁷

Within the thio-LISICON family, a large number of substitutions has been conducted following the general formula $\text{Li}_x M_{1-y} M_y' S_4$ with M = Si, Ge, Sn and M' = P, Al, Zn, Ga, Sb. Aliovalent substitutions tailor the number of Li^+ in the structure and with that the conductivity changes. ^{10,14,26,31} The substitution series $\text{Li}_{4-x} \text{Sn}_{1-x} \text{Sb}_x S_4$ was synthesized via classical solid-state reaction and mechanochemical milling incorporating Sb⁵⁺ to a different extent and

increasing the ionic conductivity into the mS·cm⁻¹-range. Moreover, the substitution of As^{5+} into Li_4SnS_4 yielded in an improved conductivity of about two orders of magnitude compared to the unsubstituted compound. Within the substitution series $Li_{3+x}As_{1-x}Ge_xS_4$, $Li_{3.334}Ge_{0.334}As_{0.666}S_4$ exhibits the highest conductivity of 1.12 mS·cm⁻¹. Furthermore, an increase about three orders of magnitude was observed when substituting Li_3PS_4 with B^{3+} . In

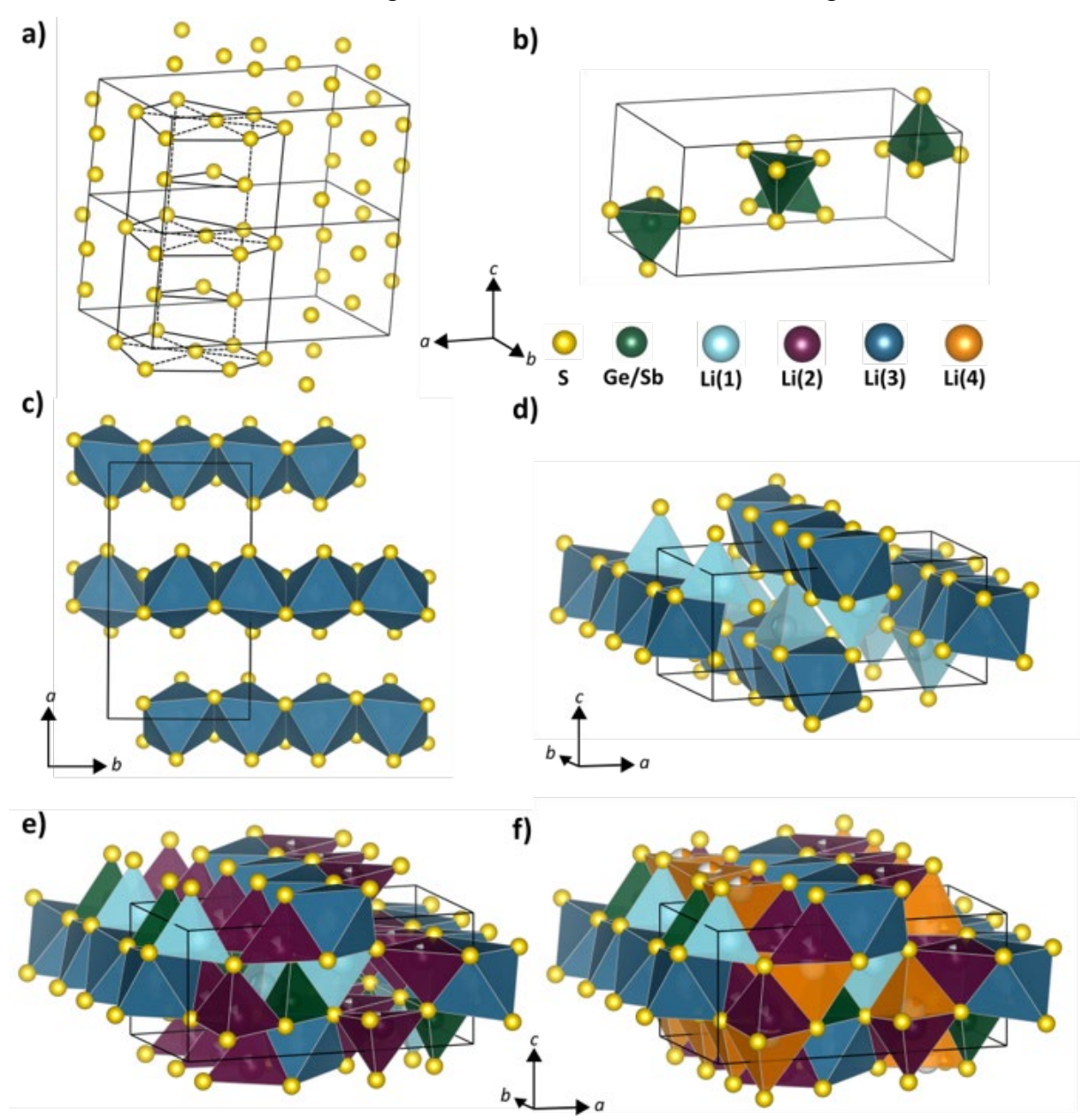


Figure 1: (a) Distorted hexagonal close-packing of the sulfur atoms in Li₄GeS₄. For simplicity all S atoms close to the packing motif are omitted. (b) Arrangement of the $(GeS_4)^{4-}$ polyhedra showing the alternating apices of the tetrahedra. (c) Chains of edge-sharing Li(3) octahedra being the main diffusion pathway in Li₄GeS₄. (d) Edge- and corner-sharing Li(1) tetrahedra and Li(3) octahedra. (e) Crystal structure of Li₄GeS₄ depicting the $(GeS_4)^{4-}$ tetrahedra and the three distinct Li⁺ positions Li(1), Li(2,) and Li(3). (f) Refined crystal structure of

 Sb^{5+} substituted Li_4GeS_4 showing an additional Li^+ position Li(4) which forms a trigonal-bipyramid with Li(2).

The highest conductivities in the thio-LISICON family are obtained for an intermediate substitution level and this evidence may lead to the conclusion that the conductivity increase is highly correlated to the Li^+ charge carrier density. However, ionic motion is affected by more than just the Li^+ charge carrier density, ³⁰ since several variables, such as polyhedral connectivity or Li^+ diffusion pathway widths, play a major role in ionic motion as well. Minafra *et al.* showed that isovalent substitutions in Li_4MCh_4 (M = Ge, Sn and Ch = S, Se) influence the ionic conductivity by tailoring the lithium polyhedral connectivity while keeping the same carrier density. ^{5,27}

Inspired by these interconnected influences, this work focusses on the substitution series Li_{4-x}Ge_{1-x}Sb_xS₄ to gain a better understanding of the interplay of Li⁺ substructure and charge carrier density. From a purely geometrical point of view, the substitution of Ge⁴⁺ with Sb⁵⁺ seems possible due to the similar radii of germanium $(r(Ge^{4+}, IV) = 0.39 \text{ Å})^{36}$ and antimony $(r(Sb^{5+}, IV) = 0.50 \text{ Å}).^{37}$ While the Li⁺ charge carrier density can easily be estimated from the stoichiometry, the Li⁺ substructure was investigated by high-resolution neutron diffraction. The so found Li⁺ substructure was then correlated to the observed changes in ionic conductivity and activation barriers as probed by impedance spectroscopy and nuclear magnetic resonance (NMR) spectroscopy. Bond valences site energy calculations and the maximum entropy method were used to gain additional insight into the Li⁺ diffusion pathways. Our results show that by incorporation of Sb⁵⁺, the unit cell volume and the total lithium polyhedral volume increase and an additional Li⁺ site is occupied. Moreover, an increasing Sb⁵⁺ content promotes the disorder and distribution of Li⁺ as revealed by the maximum entropy calculations. The enhanced Li⁺ polyhedral network connectivity further indicates much faster Li⁺ diffusion with increasing Sb⁵⁺ content altering the conductivity of about two orders of magnitude. Thus, this work demonstrates how minor compositional changes affect the anionic framework and Li⁺ distribution, leading to a strong increase in configurational entropy and a faster ionic transport in solid ionic conductors.

2. Experimental Section

Synthesis. All synthesis steps were carried out under Ar atmosphere. The samples Li_{4-x}Ge_{1-x}Sb_xS₄ (0.025 \leq x \leq 0.2) were synthesized via classic solid-state synthesis. The precursors Li₂S (Alfa Aesar, 99.9 %), Ge (Sigma Aldrich, 99.999%, trace metal basis), Sb (ChemPur, 99.999%)

and S (Acros Organics, 99.999%) were weighed stoichiometrically and an excess of 4 mol% of Li₂S was used to prevent the formation of a non-stoichiometric side phase. The mixture was ground for 15 minutes, pressed into pellets with a hand press and transferred into carbon-coated quartz ampoules that were previously dried under dynamic vacuum at 800 °C for 2 hours. Afterwards, the ampoules were sealed and the samples were annealed at 700 °C for 16 hours. The heating rate was $100 \, ^{\circ}\text{C} \cdot \text{h}^{-1}$. The samples cooled naturally and the resulting powders were hand-ground and subsequently used for characterization.

Neutron powder diffraction. Neutron powder diffraction data of $\text{Li}_{4-x}\text{Ge}_{1-x}\text{Sb}_x\text{S}_4$ (0.025 $\leq x \leq$ 0.2) containing natural Li was collected at Oak Ridge spallation neutron source (SNS, Oak Ridge National Laboratory). The PAC automatic sample changer at POWGEN diffractometer (BL-11A beamline) was used. The samples (~ 3 g) were loaded under inert atmosphere into a cylindrical vanadium can ($\emptyset = 8$ mm) which was sealed with a copper gasket to avoid air exposure during the measurement. The data collection duration was four hours per diffractogram in high-resolution mode at room temperature using a single bank with a center wavelength of 1.5 Å.

Rietveld analysis. Rietveld refinements were carried out on auto-reduced neutron diffractograms using the TOPAS-Academic V6 software package.³⁸ The structural data obtained from neutron refinements of Li₄GeS₄ from Minafra et al. were used as starting model.⁵ A convolution of pseudo-Voigt and GSAS back-to-back exponential functions was used to fit the profile shape.³⁹ Initially the (1) background, (2) scale factors of main and side phases, (3) lattice parameter and (4) the peak shape were refined. After a good fit of the profile was achieved, the (5) atomic coordinates, (6) occupancies and (7) isotropic thermal displacements parameters were refined. During the refinements, Sb was placed on Ge sites (Wyckoff 4c). The coordinates and thermal displacement of both atomic species were constrained to be the same and the occupancy was constrained to unity. Furthermore, the number of lithium atoms was constrained to the refined Sb content (Table S1). Finally, the lithium occupancy on all other possible interstitial sites was investigated. A non-zero occupancy and a positive thermal displacement parameter were indicative for lithium occupying a crystallographic site. Lithium was found on Wyckoff 8d site. This position is labeled as Li(4). Since, the fit statistics were better with Li(4) (Supporting Table S2 and Table S4), the refinements were performed including such lithium. Finally, all parameters were refined together. The only exception was the antimony-germanium ratio for a nominal composition of Li_{3.85}Ge_{0.85}Sb_{0.15}S₄, which was fixed during the last refinement cycles as the Sb occupancy was unstable, possibly due to presence of the Li₃SbS₄ side phase. The polyhedral volumes were extracted with VESTA. 40 The given errors in the following data plots correspond to one estimated standard deviation. The only exception are the polyhedral volume errors which were calculated by using the total differential of the octahedron or tetrahedron volume considering the S-S bond distances as polyhedral edges and the corresponding bond errors. For simplicity, the formula of a perfect octahedron or tetrahedron was used. The crystallographic information files (CIFs), structural tables (Figure S1, Table S3 – S7) as well as the used constraints (Table S1) are reported in the Supporting Information.

Potentiostatic electrochemical impedance spectroscopy (PEIS). AC impedance spectroscopy was used to measure the ionic conductivities. Approximately 200 mg of each sample were filled into press cells with a PEEK inlet⁴¹ and subsequently pressed uniaxially with 374 MPa for three minutes resulting in relative densities from 78% - 87% for the pellets (Table S8). The impedance measurements were conducted with a SP300 impedance analyser (Biologic) in the temperature range 233–333 K and within a frequency range of 7 MHz to 50 mHz applying an amplitude of 10 mV. The resulting impedance spectra were evaluated with RelaxIS 3 software (rhd instruments). The errors of conductivity and activation energy were calculated from fit and geometrical errors. The capacitances were calculated from the capacitances of constant phase elements according to the Brugs' formula.⁴²

Bond valence site energy (BVSE) calculations. The bond valence site energy calculation is a simple straightforward method to predict ionic motion within a crystal structure. The calculations are based on the postulate that the sum of all bond valences s_{A-X} of one atom A equals its oxidation state V(A).⁴³ The Li⁺ ion follows a pathway in which the bond valence sum mismatch $|\Delta V|$, given in arbitrary valence units, is as low as possible.⁴⁴ The valence sum mismatch can be transferred to an absolute energy scale by combining a Morse-type interaction with Coulombic repulsion.^{43,45,46} The migration pathways for Li⁺ were calculated for substitution series Li_{4-x}Ge_{1-x}Sb_xS₄ ($0 \le x \le 0.2$) with the program SoftBV V1.2.1^{43,47} using a resolution of $(0.1 \text{ Å})^3$ and a screening factor of 0.627344. The Li⁺ diffusion pathways of the refined compositions of Li₄GeS₄ and Li_{3.91}Ge_{0.91}Sb_{0.09}S₄ were compared to assess the changes in transport.

Maximum Entropy Method (MEM). The maximum entropy method can be used to extract a scattering density distribution of a crystal structure from neutron as well as X-ray diffraction data⁴⁸ using observed structure factors as an input. The calculations yield the theoretical information entropy *S*, corresponding to a certain nuclear scattering density configuration. The calculation process is iterative and the obtained scattering density distribution corresponds to

the chosen configuration with maximized information entropy. In comparison to Fourier transformation, MEM has the advantage that this method is less prone to artefacts or errors due to limited information in the data sets. ^{48,49} The program Dysnomia was used to calculate the negative nuclear density maps on the basis of the structure factors, since Li⁺ is the only element that exhibits a negative neutron scattering length. ⁴⁹

Nuclear magnetic resonance (NMR) spectroscopy. Static saturation recovery and spin-lock ⁷Li NMR experiments for the determination of T_1 and T_{1p} , respectively, as a function of temperature were performed on a Bruker AVANCE III 300 spectrometer equipped with a widebore magnet (7.05 T) using a 4 mm VTN broadband probe (Bruker). The powder samples were transferred into cylindrical zirconia rotors with an outer diameter of 4 mm under Ar atmosphere. All experiments were conducted at a Larmor frequency of 116.6 MHz with a pulse length of 2.5 µs for a 90° pulse corresponding to a nutation frequency of 100 kHz. The length of the saturation recovery delay was incremented with four steps per decade from $t_1 = 10^{-5}$ s to $t_{28} = 56.234$ s. The spin-lock ⁷Li NMR experiments employed a 20 kHz (nutation frequency) spin-lock pulse to determine $T_{1\rho}$. The spin-lock pulse duration was incremented with four steps per decade from $t_1 = 3.16 \cdot 10^{-5}$ s to $t_{16} = 0.178$ s. Static single-pulse ⁷Li NMR experiments were conducted with 64 scans at each temperature to observe the signal narrowing. The Fourier transformed ⁷Li signals were integrated in TopSpin and the signal intensity curves were fitted using exponential functions with stretching exponents. These stretching exponents reflect the non-exponential motional correlation function of ⁷Li⁺ in the investigated structurally disordered ion conductors due to a broad statistical distribution of correlation times.⁵⁰ The temperature of the samples was regulated via a nitrogen gas flow and electrical heating. From 178 K to 200 K a liquid nitrogen evaporator system was used; between 200 K and 290 K an Air Jet XR compressor-based cooling system from SP Scientific (FTS Systems) was used; from 320 K to 440 K an uncooled nitrogen gas flow was employed to stabilize the temperature. ¹H NMR spectra of methanol (178 K to 290 K) and ethylene glycol (320 K to 440 K) were recorded separately to calibrate the temperature with the occurring shifts in ⁷Li signal frequency.

3. Results

Host-framework – MS_4 *polyhedra*. The Li_{4-x}Ge_{1-x}Sb_xS₄ substitution series is prepared via a classical solid-state reaction to determine the influence of Sb⁵⁺ on the Li₄GeS₄ structure. In order to understand the influence of the substitution on the structure, Rietveld refinements against neutron diffraction data are employed. An exemplary refinement as well as all measured neutron diffraction patterns are displayed in Figure 2, all other data can be found in the

Supporting Information. First, all patterns show the formation of the Li_{4-x}Ge_{1-x}Sb_xS₄ substitution compounds, however, Li₃SbS₄ forms as a side phase when exceeding a nominal antimony substitution degree of x(Sb) = 0.1. As the fraction of impurity content increases for higher antimony contents (Figure S2), a solubility limit of Sb⁵⁺on the Ge⁴⁺ site at around 10 at.% seems to exist in the Li₄GeS₄ structure for the employed synthesis method. The refined content of Li₃SbS₄ further scales linearly with higher antimony content (Figure S2b). Considering this trend, a linear extrapolation of the Li₃SbS₄ weight fractions might indicate that Li₃SbS₄ can also be present to a small extent (< 1 wt.%) in the nominal composition of x(Sb) = 0.05. A linear correlation between the refined and nominal content of Ge4+ and Sb5+ is expected for the formation of a solid solution. However, the experimentally found Sb⁵⁺ content in Li₄GeS₄ seems to saturate at around 9 at.% of Sb on the Ge site (Figure 3a). The refined antimony content for the nominal compositions Li_{3.85}Ge_{0.85}Sb_{0.15}S₄ and Li_{3.8}Ge_{0.8}Sb_{0.2}S₄ are both 8% within the uncertainties (Table S6 and S7). The exact refined values of Sb⁵⁺ are 7.52 ± 1.57 at.% and 8.48± 2.88 at.% for Li_{3.85}Ge_{0.85}Sb_{0.15}S₄ and Li_{3.8}Ge_{0.8}Sb_{0.2}S₄, respectively. Thus, to indicate that there is actually a difference between the two samples, Li_{3.85}Ge_{0.85}Sb_{0.15}S₄ and Li_{3.8}Ge_{0.8}Sb_{0.2}S₄ are named Li_{3.92}Ge_{0.92}Sb_{0.08}S₄ and Li_{3.91}Ge_{0.91}Sb_{0.09}S₄, respectively. Therefore, the highest antimony content of 9 at.% is refined for the nominal composition of Li_{3.8}Ge_{0.8}Sb_{0.2}S₄. To account for the deviations from nominal composition, all extracted structural parameters are hereafter shown against the refined composition.

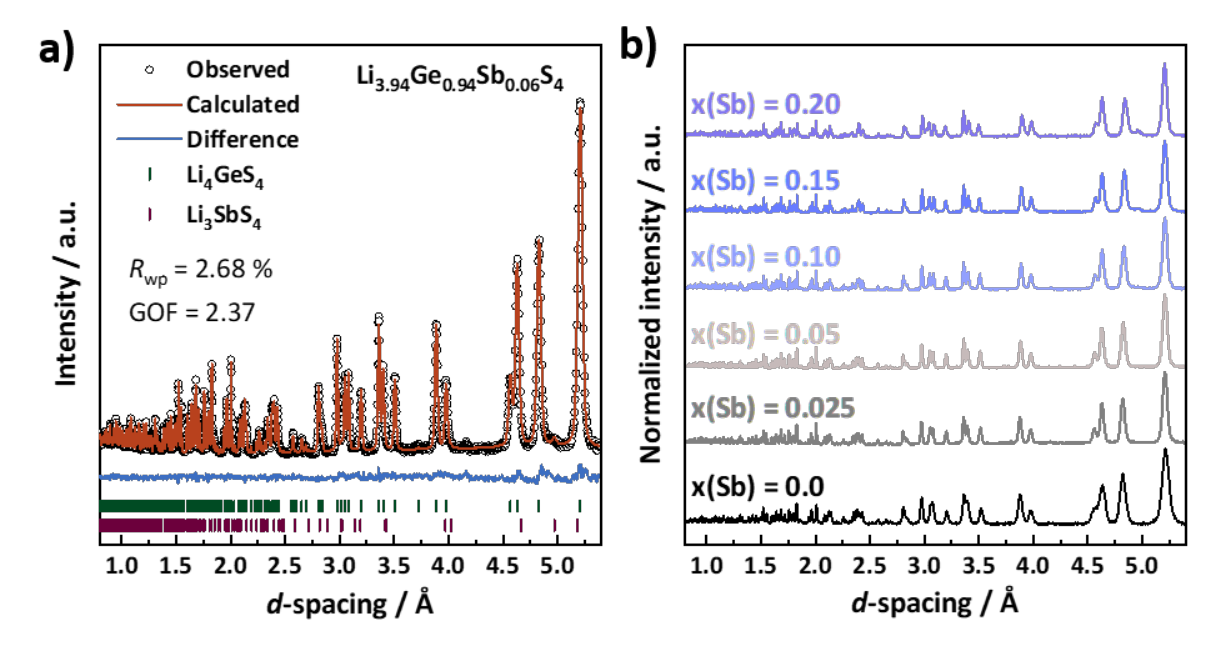


Figure 2: (a) Rietveld refinement against room temperature neutron diffraction data for $Li_{3.94}Ge_{0.94}Sb_{0.06}S_4$ corresponding to a nominal composition of $Li_{3.9}Ge_{0.9}Sb_{0.1}S_4$. An impurity of Li_3SbS_4 is found with 4.2(2) wt.%. (b) Overview of all neutron diffractograms for the $Li_{4-x}Ge_{1-x}Sb_xS_4$ substitution series.

The lattice parameters show opposing trends with increasing antimony content. While the lattice parameters b and c increase, lattice parameter a decreases (Figure 3b and 3c). Within the solid solution, the substitution results in a linear change of all lattice parameters, which then results in a unit cell expansion of 0.6% for the highest Sb⁵⁺ content in the Li₄GeS₄ structure (Figure 3d). Interestingly, when including the lattice parameters or unit cell volumes of Li₄GeS₄, a non-linear trend can be observed. This has recently been observed within the thio-LISICON class and seems to be caused by a changing lithium substructure. ^{10,14,27,31} Similar influences are expected here and will be discussed in the following sections. Overall, the linear trends for the lattice parameter and the unit cell volume against the found antimony content on the (GeS₄)⁴⁻ site indicates the successful formation of solid solutions. Nevertheless, a lower Sb⁵⁺ incorporation is found as the nominal stoichiometric compositions would have suggested.

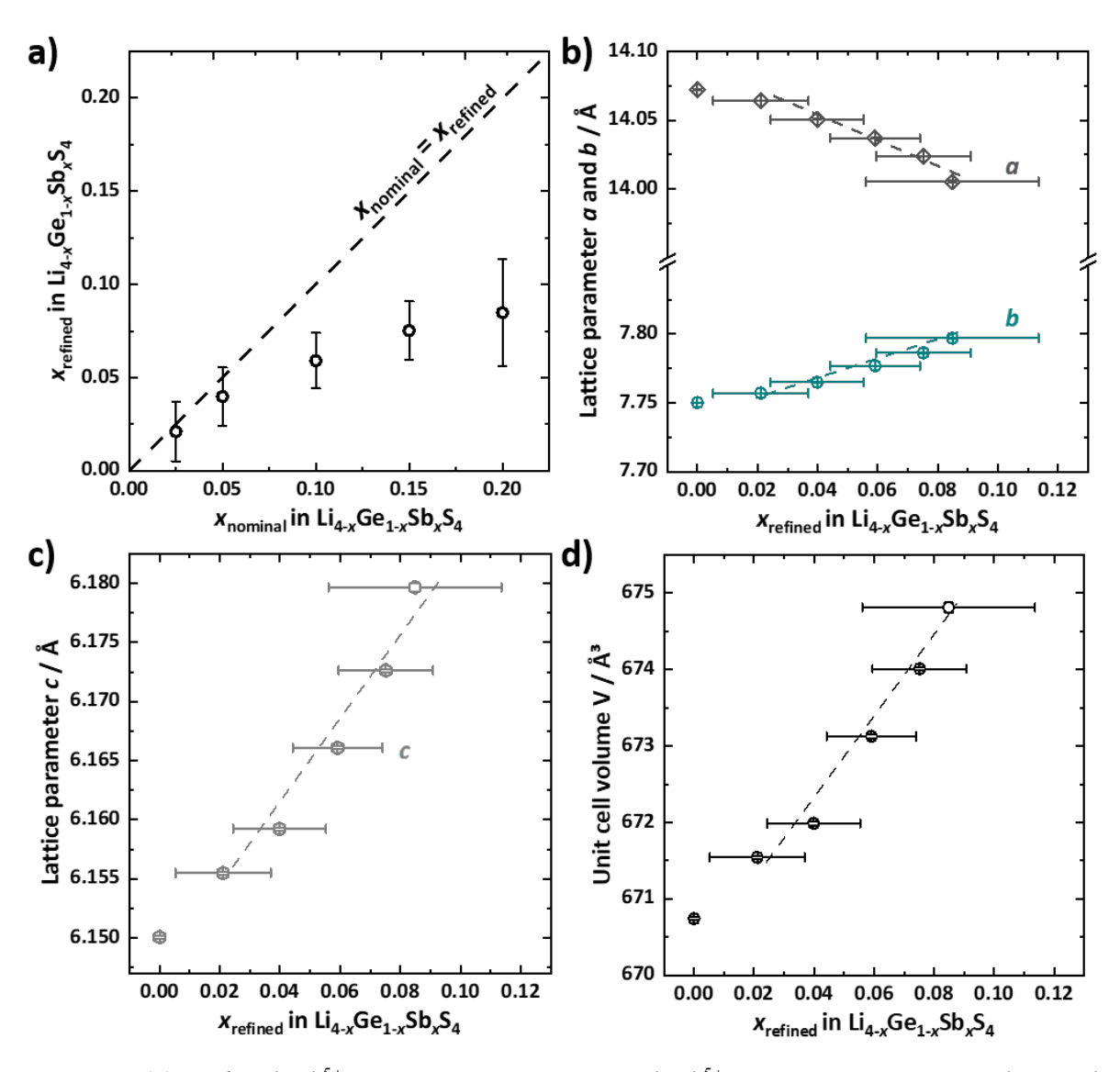


Figure 3: (a) Refined Sb^{5+} content against nominal Sb^{5+} content in $Li_{4-x}Ge_{1-x}Sb_xS_4$. The

saturation behavior suggests that only around 9 at.% Sb seem to be incorporated into the structure. The dashed line represents the expected trend for a full Sb^{5+} incorporation. (b) and (c) The lattice parameters b and c are increasing, while lattice parameter a is decreasing. (d) The unit cell volume expansion follows a linear trend when Sb^{5+} is incorporated in Li_4GeS_4 . All trends reveal a deviation from a linear trend for unsubstituted structure from all other samples. The lines shown are guides-to-the-eye.

Lithium substructure. The lithium substructure was investigated by Rietveld refinements against neutron diffraction data to gain further insights into the underlying transport processes from a structural point of view and to understand the non-linear change in the lattice parameters upon initial Sb⁵⁺ substitution. The first noticeable structural change is that the lithium substructure of the substitution series Li_{4-x}Ge_{1-x}Sb_xS₄ differs from the lithium substructure of Li₄GeS₄. To be precise, one additional lithium position Li(4) can be found when Ge⁴⁺ is partially substituted with Sb⁵⁺ (Figure 1e and 1f), possibly explaining the deviation of Li₄GeS₄ from a linear trend of the lattice parameter and volume between unsubstituted and Sb⁵⁺ substituted Li₄GeS₄. The Li(4) site is edge- and face-sharing with Li(2) forming a trigonal-bipyramid and therefore further improving the lithium polyhedral connection in the *ac*-plane (Figure 1f). This additional position reflects a redistribution of Li(2) in its tetrahedral position towards the sharing position along the *z*-direction. With this additional Li⁺ site, the Li⁺ substructure of the Li_{4-x}Ge_{1-x}Sb_xS₄ solid solution series is the same as the Li⁺ substructure of Li₄GeSe₄. Tin which the lithium ions are distributed over these four distinct crystallographic sites.

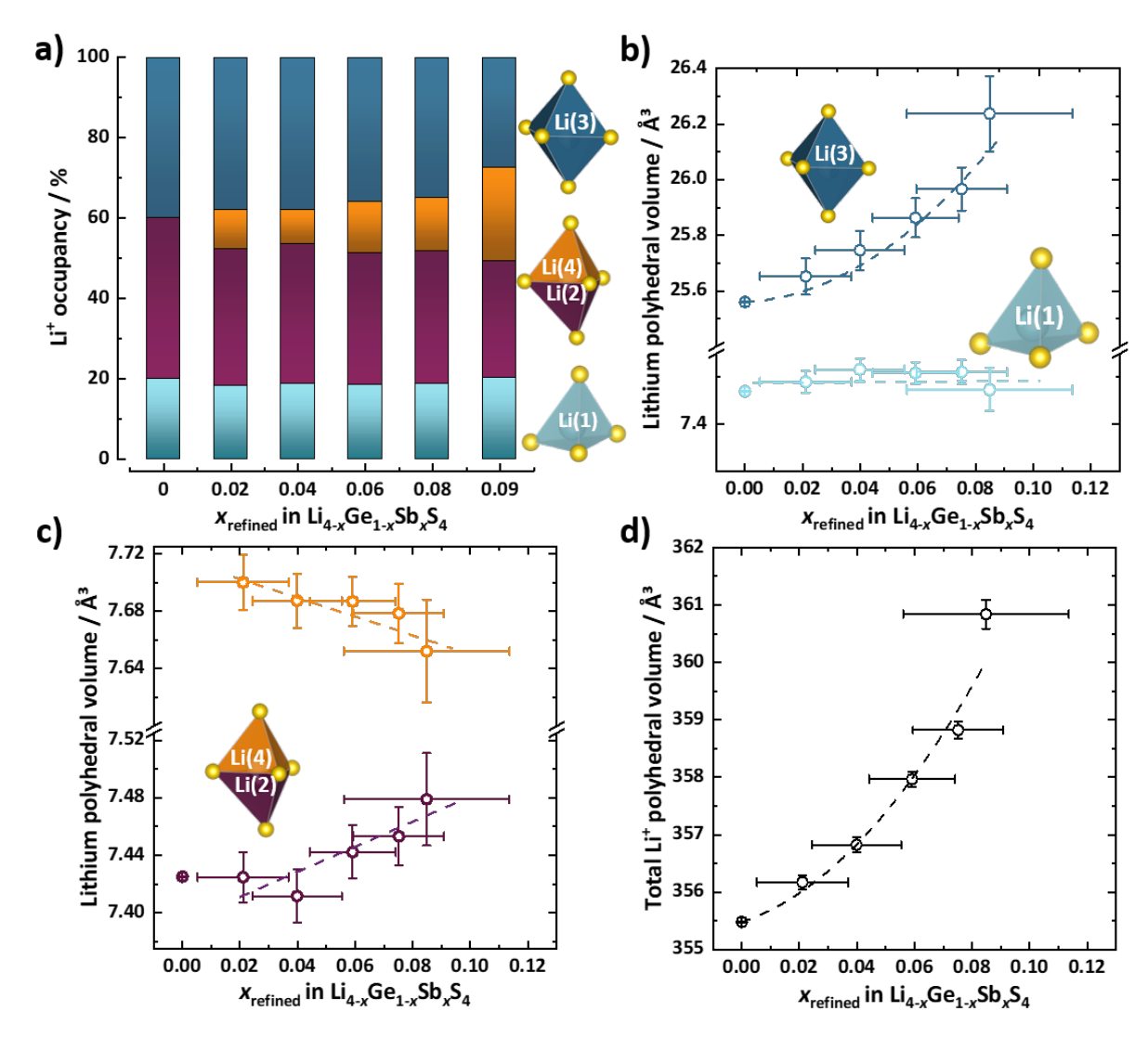


Figure 4: (a) Lithium distribution for Li^+ within the $Li_{4-x}Ge_{1-x}Sb_xS_4$ substitution series. The occupancy of Li(1) remains almost unaffected by the substitution. The occupancy of Li(2) and Li(3) decreases whereas the occupancy on Li(4) site increases over the whole substitution series increases. (b) The Li(1) tetrahedron volume is unaffected by the substitution, while the Li(3) octahedron volume increases the most of all polyhedral volumes. (c) The tetrahedron volume of Li(2) is increasing while the Li(4) volume decreases upon Sb^{5+} substitution (d) Total Li^+ polyhedral volume increase upon introduction of Sb^{5+} . All dashed lines are guides-to-the-eye.

The polyhedra volumes of LiS_x octahedra and tetrahedra as well as their occupancy are shown in Figure 4 for the $Li_{4-x}Ge_{1-x}Sb_xS_4$ solid solution. The occupancy of Li(1) remains close to unity, while the occupancy of Li(3) decreases with increasing Sb^{5+} content (Figure 4a). In addition, the lithium occupancy is redistributed from Li(2) to Li(4) (Figure 4a). This preference of Li^+ to occupy Li(4) can be visualized by plotting the change in occupancy against the refined Sb^{5+} content, indicating that the Li^+ on Li(4) comes mainly from Li(2) and to a smaller extent from Li(3) (Figure S3). The redistribution of Li^+ may be attributed to the change in polyhedral

volumes or vice versa, as well as to a higher Li⁺ mobility, which can be induced by lowering the carrier density. Li(2) and Li(4) are in close proximity (< 1 Å) and cannot be occupied at the same time due to repulsive electrostatic interaction. While in this study Li(2) and Li(4) are considered as two distinct sites, one may regard them as a single position with a smeared-out Li⁺ distribution. In addition to the occupancy changes, the polyhedral volume of Li(2) is increasing ($\sim 0.8\%$), while the tetrahedron of Li(4) is shrinking ($\sim 0.6\%$) (Figure 4c). The changing volume may be caused by the changing positive charge in the center of the polyhedron, further corroborating the occupation of the additional Li(4) site. The Li(1) tetrahedron seems to retain its volume over the whole substitution range. The most pronounced change in polyhedral volumes is found for the Li(3) octahedron with an increase in polyhedral volume of 2.6% (Figure 4b). Furthermore, the total lithium polyhedral volume, which is the sum of all Li⁺ polyhedral volumes, increases in a quadratic fashion with higher Sb⁵⁺ content (Figure 4d). For all substitutions the Li(4) polyhedron was included to increase comparability in the volume expansion of the Li⁺ polyhedra. Thus, the Sb⁵⁺substitution leads to a volume expansion of the Li⁺ substructure and alters the Li⁺ distribution. With $x(Sb^{5+}) > 0$ the Li⁺ disorder, as defined by the largely varying Li⁺ occupancies on the four crystallographic sites, is subsequently changing starting from Li₄GeS₄.

Ionic transport characterized by impedance spectroscopy. The influence of Sb⁵⁺ substitution on ionic transport is probed by PEIS. Since Li₄GeS₄ seems to be much more ionically resistive, a comparison of the impedance spectra of Sb⁵⁺ containing samples and Li₄GeS₄ can be found in the Supporting Information (Figure S4). The impedance spectra consist of a semicircle and the blocking behavior of the metal contacts (Figure 5a) and can be fit with a parallel resistor-constant phase element in series with a constant phase element (see inset Figure 5a). The semicircle is assigned to bulk resistances based on capacitances of 16 pF to 31 pF as well as non-ideal alpha values of 0.75 to 0.90.^{42,51} However, the obtained capacitances and alpha values indicate the presence of a second process, which could be connected to grain-boundaries due to the introduction of Sb⁵⁺ (Figure S5). Thus, the reported conductivities represent total conductivities.

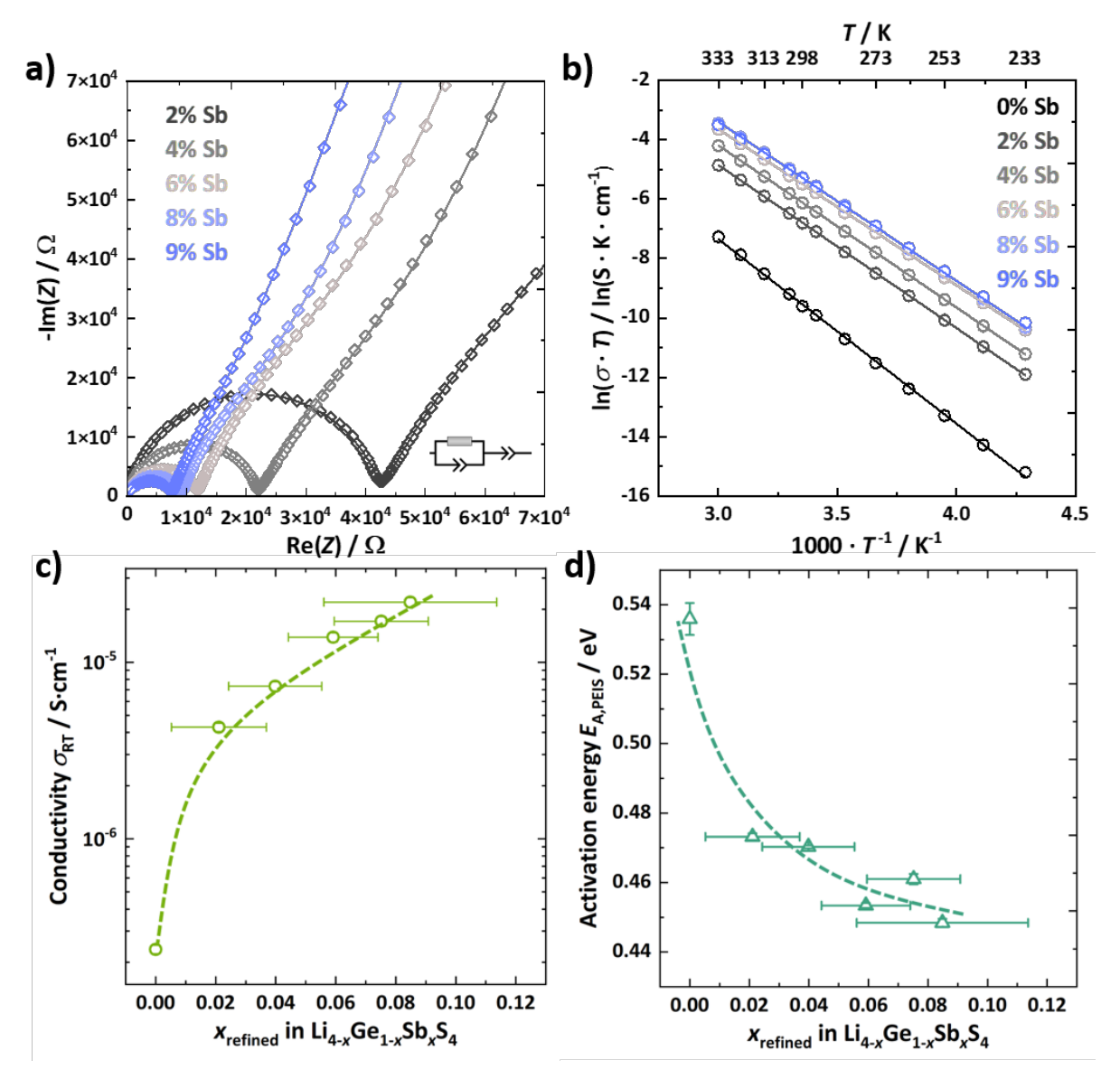


Figure 5: (a) Nyquist plots of the $Li_{4-x}Ge_{1-x}Sb_xS_4$ substitution series with x > 0 at room temperature. (b) All samples exhibit Arrhenius behavior over the measured temperature range indicated by the linearity of the Arrhenius plot. (c) The conductivity improves upon Sb^{5+} substitution by about two orders of magnitude. The best conductivity was reached at ~ 9 at.% Sb. (d) Initially. the activation energy $E_{a,PEIS}$ drops strongly and then, is further decreased reaching its minimum for 9 at.% Sb. The solid and the dashed lines are actual fits and guidesto-the-eye, respectively. In (c) and (d) the y-error bars have the magnitude of the symbols.

All samples of the $\text{Li}_{4-x}\text{Ge}_{1-x}\text{Sb}_x\text{S}_4$ substitution series exhibit Arrhenius behavior over the measured temperature range of $-40\,^{\circ}\text{C}$ to $60\,^{\circ}\text{C}$ (Figure 5b). The conductivity (Figure 5c) shows a steep increase over two orders of magnitude from $2.4\cdot10^{-7}\,\,\text{S}\cdot\text{cm}^{-1}$ for Li_4GeS_4 to $2.2\cdot10^{-5}\,\,\,\text{S}\cdot\text{cm}^{-1}$ for $\text{Li}_{3.91}\text{Ge}_{0.91}\text{Sb}_{0.09}\text{S}_4$. Li_3SbS_4 increases as a side phase with higher substitution level, however the compound cannot correlated to the increase in conductivity since

the material itself exhibits a low conductivity of $4.8 \cdot 10^{-9} \text{ S} \cdot \text{cm}^{-1}$ (Figure S6).⁵² Furthermore, the activation energy $E_{\text{a,PEIS}}$ reflects the opposite trend showing a strong decrease of about 0.1 eV from the non-substituted sample to $x_{\text{ref}}(\text{Sb}) = 0.09$ as shown in Figure 5d.

Li⁺ dynamics characterized by ⁷Li NMR spectroscopy. While impedance spectroscopy captures the bulk Li⁺ motion as the observable Li⁺ ionic conductivity, NMR spectroscopy has the possibility to distinguish Li⁺ jump processes in the bulk material on different time scales. ⁵³ ⁷Li spin-lattice relaxometry in the laboratory (T₁) and rotating frame (T_{1p}) as well as the temperature dependency of the ⁷Li central transition line shape for Li₄GeS₄ and the highest substituted Li_{3.91}Ge_{0.91}Sb_{0.09}S₄ are for this reason measured to obtain activation energies and the onset of Li⁺ motion in the slowest and fastest ionic conductor of the substitution series. Moreover, static ⁷Li NMR static line width analysis allows to monitor the change in Li⁺ diffusivity (Figure 6a). ⁵⁴ The observed narrowing of the ⁷Li central transition signal of Li₄GeS₄ and Li_{3.91}Ge_{0.91}Sb_{0.09}S₄ with increasing temperature corresponds to progressively increasing Li⁺ motion. At low temperatures in the rigid lattice regime the ⁷Li line width is determined by the strength of the ⁷Li-⁷Li dipole-dipole couplings. Increasing the temperature leads to motional averaging of these dipole couplings due to increased Li⁺ jump rates resulting in a substantial narrowing of the ⁷Li central transition signal. At very high temperatures the motional narrowing is completed and the line width is purely determined by magnetic field inhomogeneities. ^{50,54}

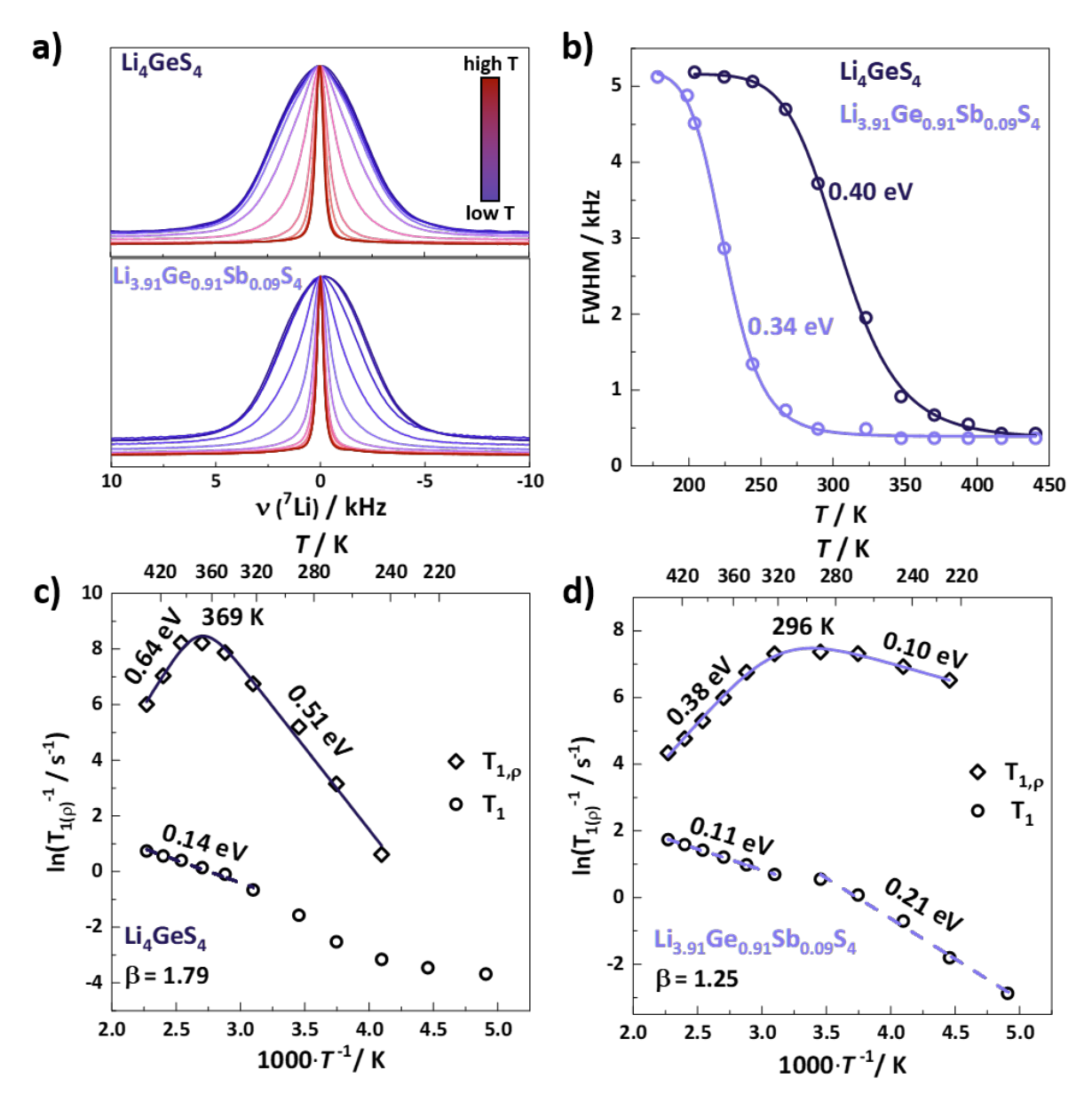


Figure 6: (a) 7Li NMR spectra for Li₄GeS₄ and Li_{3.91}Ge_{0.91}Sb_{0.09}S₄ as a function of temperature from 178 K to 440 K as indicated by the color gradient. (b) Motional narrowing curves for Li₄GeS₄ and Li_{3.91}Ge_{0.91}Sb_{0.09}S₄ obtained by plotting the full width at half maximum (FWHM) of the 7Li signal in (a) versus the temperature. The Sb⁵⁺ substituted compound exhibits the onset of line narrowing at a significantly lower temperature indicating faster Li⁺ dynamics. (c) and (d) 7Li T₁ and T₁ $_P$ relaxometry measurements for Li₄GeS₄ and Li_{3.91}Ge_{0.91}Sb_{0.09}S₄ indicating a non-Arrhenius behaviour at low temperatures for T₁. The 7Li T₁ $_P$ relaxometry measurements show asymmetric rate peaks likely corresponding to several superimposed motional processes.

The change in Li⁺ motion can be visualized by following the full width at half maximum (FWHM) of the ⁷Li central transition signal versus the temperature (Figure 6b). The resulting motional narrowing curve for Li_{3.91}Ge_{0.91}Sb_{0.09}S₄ is clearly shifted to lower temperatures

compared to Li₄GeS₄, indicating that the onset of Li⁺ motion for the Sb⁵⁺ substituted sample occurs at significantly lower temperatures. Furthermore, the activation energy $E_{a,HB}$ can be extracted from the motional narrowing curves via the phenomenological model reported by Hendrickson and Bray (Table 1).⁵⁵ On this basis, the activation energy $E_{A,HB}$ can be observed to decrease about 15% from Li₄GeS₄ to Li_{3.91}Ge_{0.91}Sb_{0.09}S₄, corroborating the trends found using impedance spectroscopy.

Table 1: Comparison of activation energy by potentiostatic impedance spectroscopy $E_{A,PEIS}$, central line shape analysis $E_{A,HB}$, 7Li spin-lattice relaxation rates in the laboratory frame $E_{A,1}$ and 7Li spin-lattice relaxation rates in the rotating frame (high- and low-temperature flank $E_{A,BPP\ high}$ and $E_{A,BPP\ low}$, respectively.

	E _{A,PEIS}	Ел,нв	<i>E</i> _{A,1}	EA,BPP high	EA,BPP low
	/ eV	/ eV	/ eV	/ eV	/ eV
Li ₄ GeS ₄	0.53	0.40	0.14	0.64	0.51
Li _{3.91} Ge _{0.91} Sb _{0.09} S ₄	0.44	0.34	0.11	0.38	0.10
Li ₄ GeS ₄	0.55	0.43	0.17	0.53	0.56
(Hogrefe et al.) ⁵⁶	0.55	0.43	0.17	0.55	0.50

The observation of Li⁺ motion characterized by ionic jump rates in the MHz range and kHz range is achieved by measuring 7 Li spin-lattice relaxation rates in the laboratory frame T_1^{-1} and the rotating frame $T_{1\rho}^{-1}$, respectively. 54,57 The Arrhenius representation of the data for T_1^{-1} and $T_{1\rho}^{-1}$ are displayed in Figure 6c and 6d. The relaxation rates $T_{1\rho}^{-1}$ for Li₄GeS₄ and Li_{3.91}Ge_{0.91}Sb_{0.09}S₄ reveal Arrhenius curves with asymmetric flanks, in which the high- and low-temperature flanks correspond to long-range and to short-range Li⁺ motion, respectively. 58 The maximum rotating frame relaxation rate of the Sb⁵⁺ substituted compound is at 296 K, while the maximum of Li₄GeS₄ is at 369 K suggesting faster jump rates for the Li_{3.91}Ge_{0.91}Sb_{0.09}S₄, complementing the observations from the static 7 Li linewidth analysis. The asymmetry of $T_{1\rho}^{-1}$ Arrhenius curve for Li_{3.91}Ge_{0.91}Sb_{0.09}S₄ is clearly larger than that for Li₄GeS₄ indicating a much broader distribution of jump rates in Li_{3.91}Ge_{0.91}Sb_{0.09}S₄ that corresponds to superimposed processes which cannot be separated. 50 For the T_1^{-1} measurements, which capture faster motional processes than $T_{1\rho}^{-1}$, no distinct maximum is observed. It is reasonable to assume that a maximum relaxation rate T_1^{-1} could be observed at higher temperatures. However, the activation energy $E_{a,1}$ can be determined for specific linear temperature intervals for the T_1^{-1}

measurements and the modified Bloemberg-Purcell-Pound (BPP) model is used to determine the activation energies $E_{A,BPP}$ from the $T_{1\rho}^{-1}$ measurements. S8,59 Clearly a decrease in activation energy going from Li₄GeS₄ to Li_{3.91}Ge_{0.91}Sb_{0.09}S₄ is observed when comparing both NMR relaxation methods and the PEIS measurement indicating that Li⁺ jump rates increase upon Sb⁵⁺ introduction. (cf. Table 1). The activation energy $E_{a,BPP \, high}$ for the high-temperature flank of $T_{1\rho}^{-1}$ curve decreases by about 40% going from Li₄GeS₄ to Li_{3.91}Ge_{0.91}Sb_{0.09}S₄. We note that, Hogrefe *et al.* determined a smaller $E_{a,BPP \, high}$ for the high-temperature flank of Li₄GeS₄ and observed two overlapping asymmetric rate $T_{1\rho}^{-1}$ curves for Li₄GeS₄, which they assigned to a stepwise activated diffusion being absent in this work. Nevertheless, here the activation energy $E_{A,BPP \, low}$ decreases about 80% indicating a heavily improved short-range Li⁺ transport.

Lithium-ion diffusion pathways. In order to better understand the lithium-ion diffusion pathways and the lithium-ion substructure, a simplified substructure is shown as a two-dimensional projection of the Li⁺ polyhedra in Figure 7. The Li⁺ diffusion pathways are well studied for Li₄GeS₄,^{5,27} in which long-range Li⁺ diffusion occurs *via* the edge-sharing Li(3) octahedra along the *b*-axis (Figure 1c).^{5,27,28} The *ac*-plane does not allow for a continuous Li⁺ diffusion due to the missing direct connection between the Li⁺ polyhedra, but localized jumps between the face-sharing Li(2) tetrahedron and Li(3) octahedron are possible (Figure 7a).^{5,27}

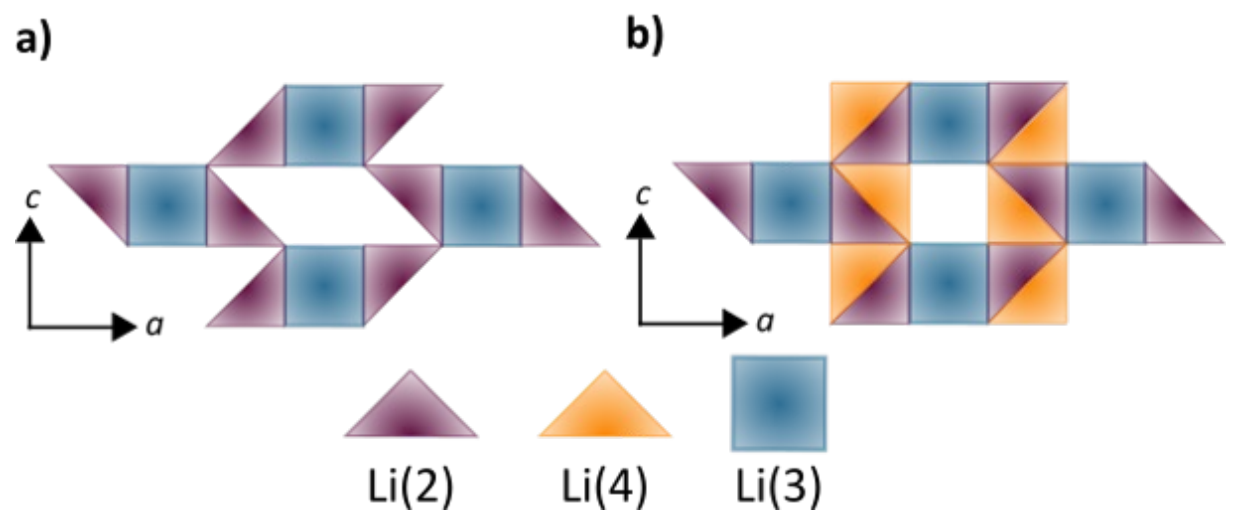


Figure 7: Schematic 2D representations illustrating the Li^+ connectivity of structural motifs in the ac-plane omitting other polyhedral and atoms of the structure. (a) Li_4GeS_4 and (b) Li^+ substructure of Sb^{5+} substituted Li_4GeS_4 that is better connected within the ac-plane compared to Li_4GeS_4 due to the introduction of Li(4).

The introduction of Li(4) into the Li_{4-x}Ge_{1-x}Sb_xS₄ structure enhances the Li⁺ polyhedral connection in the *ac*-plane (Figure 7b). As mentioned, Li(2) and Li(4) are face-sharing and form

a trigonal-bipyramid, where both Li⁺ ions are displaced away from the center towards the shared face. This arrangement is probably favourable for improving ionic transport at least on a local level, corresponding to a smeared out nuclear density over both sites.⁶⁰

To corroborate the hypothesis that the redistribution of Li⁺ despite having a lower carrier density leads to better diffusivity, the analysis of nuclear scattering densities calculated using MEM evaluation of the neutron diffraction data is carried out for Li⁺ in Li₄GeS₄ and the highest Sb⁵⁺ substituted compound Li_{3.91}Ge_{0.91}Sb_{0.09}S₄. The data show a clear difference in Li⁺ distribution between the unsubstituted and highest substituted compound presented in form of the iso-surfaces (Figure 8a). Thus, while Li₄GeS₄ is characterized by more localized Li⁺ distribution, Li⁺ is distributed more over its multiple sites in in Li_{3.91}Ge_{0.91}Sb_{0.09}S₄ where the disordered linear Li(3)-Li(3) and Li(2)-Li(4) units enable Li⁺ movement and distribution throughout the unit cell. (cf. Figure 8b and 8c).

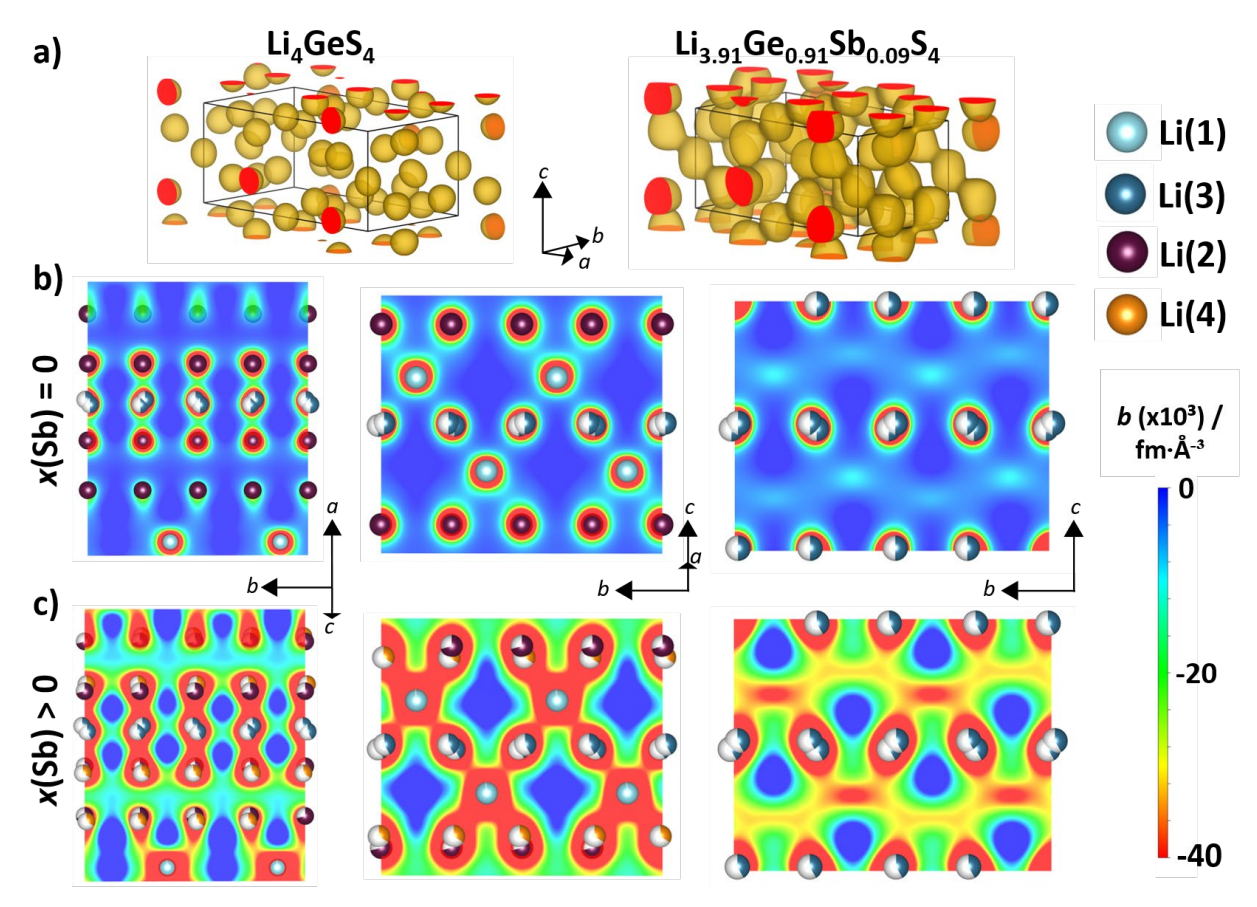


Figure 8: (a) Illustration of Li^+ iso-surface of Li_4GeS_4 and $Li_{3.91}Ge_{0.91}Sb_{0.09}S_4$ at 0.05 fm·Å⁻³ iso-surface level. (b) Display of different slices depicting the Li^+ probability calculated for Li_4GeS_4 . The Li^+ distribution of Li_4GeS_4 is localized over the different Li^+ sites. (c) Depiction of Li^+ probability slices for $Li_{3.91}Ge_{0.91}Sb_{0.09}S_4$ showing a stronger Li^+ distribution.

While Li(1), Li(2) and Li(3) scattering densities are localized in Li₄GeS₄, the incorporation of Sb⁵⁺ introduces the Li⁺ disorder over these Li⁺ sites as well as to the additional Li(4) site (Figure S3), showing a clear connection between them (Figure 8c). In other words, ionic motion between Li(1), Li(2)/Li(4) and Li(3) seems to occur more easily. Additionally, the diffusion pathway along the *b*-axis via Li(3) exhibits a transition via interstitial sites including Li(1). Thus, the connectivity is improved since Li(1) links to both Li(3) and Li(2)/Li(4) sites. Transport in the *ac*-plane occurs via the linear Li(2)-Li(4) units. As indicated by ⁷Li spin-lattice relaxometry in the rotating frame, the short-range Li⁺ transport is facilitated for higher Sb⁵⁺ contents indicated by a reduction of activation energy of 80% going from Li₄GeS₄ to Li_{3.91}Ge_{0.91}Sb_{0.09}S₄. This fits well with the newly found Li(4) position and the Li⁺ disorder over the four Li⁺ sites upon Sb⁵⁺ substitution and the therewith increasing Li⁺ disorder. More precisely, the Li⁺ occupancy seems to shift mostly from Li(2) and Li(3) to Li(4). Li(2) shares faces with Li(4) and Li(3) and is located right in between Li(4) and Li(3), thus a redistribution of Li⁺ on a local level is highly possible (Figure S7).

Structure-property relationships. Overall, the introduction of Sb⁵⁺ into Li₄GeS₄ and with it the introduction of an additional Li⁺ position and the subtle (< 3%) reduction in Li⁺ carrier density, clearly leads to a stronger, more uniform Li⁺ distribution, higher conductivity and lower barriers for ionic transport. Unclear is, however, on what scale the different structural and compositional influences alter the ionic conductivity, since just a superposition of them is measurable. In this section we will try to discern a few suggested influences.

Unit cell expansion and total Li^+ polyhedral volume. In most cases, an enlargement of the unit cell is associated with enhanced ionic motion. The increase in volume within the substitution series $Li_{4-x}Ge_{1-x}Sb_xS_4$ due to higher Sb^{5+} content may be beneficial for ionic motion (Figure 5c). Besides a volume change, a change in electrostatic interactions is expected since Ge^{4+} is replaced by Sb^{5+} on the $(MS_4)^{n-}$ polyhedral unit. To probe a change in Coulombic interactions, the Li^+ diffusion pathway and corresponding activation energies $E_{A,BVSE}$ are calculated via bond valence site energy (BVSE) calculations (Figure 9a and S8). The calculated Li^+ diffusion pathway is the same when introducing Sb^{5+} (Figure S8). Similar to the activation energy $E_{A,PEIS}$, $E_{A,BVSE}$ decreases with the unit cell volume (Figure 9a). However, the decrease for $E_{A,BVSE}$ is close to linear and not as pronounced as the decrease of $E_{A,PEIS}$. Nonetheless, this indicates that the attractive Columbic interactions between Li^+ and the $(MS_4)^{n-}$ polyhedral units are reduced, since the distance between the ions is enlarged due to the expansion of the Li^+ polyhedral network (Figure 4d) and a lower polyanionic charge is found. However, the volume effects

from the small unit cell expansion as well as purely electrostatic interactions may not sufficiently describe the change in Li⁺ distribution indicated by a new Li⁺ site and the corresponding change in ionic transport.

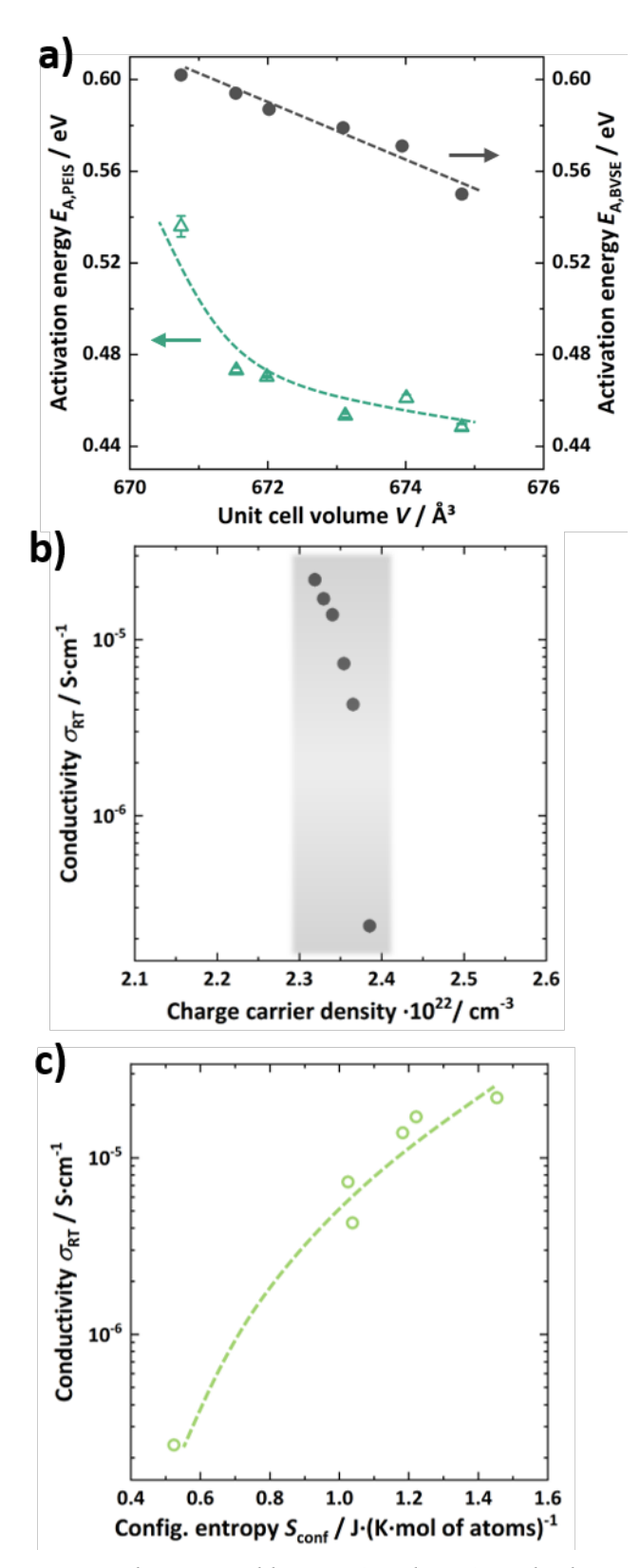


Figure 9: (a) Activation energy determined by PEIS and BVSE calculations that both decreases with increasing unit cell volume. (b) The charge carrier density changes less than 3%, however,

the ionic conductivity is altered over two orders of magnitude depicting that the carrier density may not be a major contributing factor in the enhancement of ionic motion (c) A positive correlation between the configurational entropy and the room-temperature ionic conductivity is found showing the positive influence of structural disorder on ionic motion. The dashed lines represent guides-to-the-eye.

Li⁺ charge carrier density and Li⁺ disorder. The introduction of Sb⁵⁺ in Li₄GeS₄ somewhat reduces the charge carrier density and a faster ionic motion was found (Figure 5c).) In this work, the optimum Li⁺ density, assuming that all Li⁺ participate in the diffusion process, 61 is associated with the highest ionic conductivity corresponding to ~2.32·10²² carriers·cm⁻³ for $x_{\text{ref}}(Sb) = 0.09$ (Figure 9b). On the one hand, the Li⁺ carrier density decreases only about 3% indicating that it may not be a major influence on conductivity. On the other hand, the slight removal of Li⁺ may be a contributing factor to the Li⁺ disorder within the unit cell. MEM calculations reveal that within Li_{3.91}Ge_{0.91}Sb_{0.09}S₄, the Li⁺ sites are better connected and the Li⁺ distribution is stronger when compared to Li₄GeS₄ (Figure 8c). Additionally, the NMR relaxation measurements indicate easier transport on a local level facilitating the different Li⁺ motion between the Li⁺ sites, especially between Li(2), Li(4) and Li(3) which are now well connected (Figure S7). Thus, we hypothesize that it is the Li⁺ distribution corresponding to structural disorder, rather than the subtle change in carrier concentration, that plays the largest role in the magnitude of ionic conductivity. Configurational entropy is an intuitive metric for structural disorder, and provides a means to quantitatively connect disorder to the ionic conductivity. In particular, the configurational entropy describes, in this case, statistically the distribution of Li⁺ onto the different crystallographic sites. The maximal configurational entropy is reached when a uniform distribution is achieved, i.e. every site is half occupied. Each entropic species has to be defined as an element to avoid loss of information regarding the configuration entropy.⁶² The sublattice model (SL) defines the configurational entropy as the following. 62,63

$$S_{\text{SL}}^{\text{config}} = \frac{-R \cdot \sum_{S} \sum_{i} a^{S} \cdot X_{i}^{S} \cdot \ln(X_{i}^{S})}{\sum_{S} a^{S}}$$

The parameter a^S corresponds to the multiplicity of the crystallographic site S, X_i^S describes the occupancy of species i on the crystallographic site S and R is the molar gas constant. This model should be able to capture the occupancy changes and thus, creates an opportunity to link structural disorder to observed sample properties, in this case connect the Li⁺ disorder indirectly

to the conductivity.⁶⁴ However, one has to keep in mind that an ideal configurational entropy is calculated neglecting inhomogeneous mixing within the structure.⁶²

The biggest change in configurational entropy is observed for the incorporation of Sb⁵⁺ into the crystal structure, which concurrently introduces a new Li⁺ site Li(4) and results in the highest increase in ionic conductivity. Afterwards, the configurational entropy and the ionic conductivity increases steadily further, but to a smaller extent, due to the varying Ge⁴⁺/Sb⁵⁺ occupancy and the change in distribution in Li⁺ occupancy over the four Li⁺ different sites. Using the configurational entropy as a descriptor for the occurring structural changes does not necessarily mean that it is the entropy itself that affects the transport. Rather, the Li⁺ ions become better distributed within the crystal structure and thus, Li⁺ is able to exchange between different sites more easily in the Sb⁵⁺ substituted compounds.

Overall, the idea that structural disorder is connected to ionic conductivity has been shown to exist in a variety of systems such as $\text{Li}_{4-x}\text{Zn}_{1-x}\text{Ga}_x(\text{PO}_4)_2$, ⁶⁵ $\text{Li}_{3.25}[\text{Si}_{0.25}\text{P}_{0.75}]\text{S4}$, ⁶⁶, Li_3ErCl_6 , ⁶⁷ $\text{Li}_3\text{YCl}_6^{16,68}$ or $\text{Li}_6\text{PS}_5\text{X}$ (X = Cl, Br, I)^{9,69,70} by monitoring the changing occupancies of host-framework atoms or lithium ions. These studies also showed that any degree of higher disorder, achieved via substitution or different syntheses, is beneficial for the ionic conductivity. ^{16,70} In addition to host-framework disorder, a disordered Li⁺ sublattice can be intrinsically present in the sample or it is induced by substitution to promote ionic conductivity. ^{64,66,71,72} Thus, this work highlights the strong importance of disorder on the ionic transport in materials.

4. Conclusion

The substitution series $\text{Li}_{4-x}\text{Ge}_{1-x}\text{Sb}_x\text{S}_4$ ($0 \le x_{\text{nominal}} \le 0.2$) was synthesized via classical solidstate synthesis. The introduction of Sb^{5+} results in an anisometric expansion of the unit cell and the introduction of a new Li^+ site Li(4), which enhances the Li^+ polyhedral connectivity locally in the ac-plane. Thus, the overall Li^+ sublattice suggests a higher Li^+ diffusion pathway dimensionality in $\text{Li}_{4-x}\text{Ge}_{1-x}\text{Sb}_x\text{S}_4$ than in Li_4GeS_4 . The latter is corroborated by MEM calculations of the Li^+ nuclear scattering density distribution and NMR measurements of the ionic transport, showing a higher Li^+ probability between the different Li^+ sites and a greatly reduced activation energy for short-range motion, respectively. An increasing configurational entropy reflects a higher structural disorder within the Li^+ sublattice induced by Sb^{5+} substitution all of which can be linked to an increase in conductivity. Finally, this work reinforces that subtle compositional changes in in $\text{Li}_{4-x}\text{Ge}_{1-x}\text{Sb}_x\text{S}_4$ can strongly influence the observable conductivity due to generated structural disorder by substituting aliovalently.

Acknowledgments

The research was supported by the Federal Ministry of Education and Research (BMBF) within the project Festbatt under grant number 03XP0430F. B.W. is member of the International Graduate School for Battery Chemistry, Characterization, Analysis, Recycling and Application (BACCARA), which is funded by the Ministry for Culture and Science of North Rhine Westphalia, Germany. A portion of this research used resources at the Spallation Neutron Source, a DOE Office of Science User Facility operated by the Oak Ridge National Laboratory.

Supporting Information

The Supporting Information includes X-ray diffraction data, neutron diffraction data, Rietveld refinement results, the crystallographic information files (CIFs), room-temperature impedance data, the change in alpha(CPE), room-temperature conductivities for higher Sb⁵⁺ substitutions and calculated Li⁺ diffusion pathways by BVSE.

References

- (1) Janek, J.; Zeier, W. G. A Solid Future for Battery Development. *Nat. Energy* **2016**, *1* (9), 16141.
- (2) Zhang, Z.; Shao, Y.; Lotsch, B.; Hu, Y. S.; Li, H.; Janek, J.; Nazar, L. F.; Nan, C. W.; Maier, J.; Armand, M.; Chen, L. New Horizons for Inorganic Solid State Ion Conductors. *Energy Environ. Sci.* **2018**, *11* (8), 1945–1976.
- (3) Zheng, F.; Kotobuki, M.; Song, S.; Lai, M. O.; Lu, L. Review on Solid Electrolytes for All-Solid-State Lithium-Ion Batteries. *J. Power Sources* **2018**, *389*, 198–213.
- (4) Wang, Y.; Richards, W. D.; Ong, S. P.; Miara, L. J.; Kim, J. C.; Mo, Y.; Ceder, G. Design Principles for Solid-State Lithium Superionic Conductors. *Nat. Mater.* **2015**, *14* (10), 1026–1031.

- (5) Minafra, N.; Culver, S. P.; Li, C.; Senyshyn, A.; Zeier, W. G. Influence of the Lithium Substructure on the Diffusion Pathways and Transport Properties of the Thio-LISICON Li₄Ge_{1-x}Sn_xS₄. *Chem. Mater.* **2019**, *31* (10), 3794–3802.
- (6) Schlem, R.; Ghidiu, M.; Culver, S. P.; Hansen, A.; Zeier, W. G. Changing the Static and Dynamic Lattice Effects for the Improvement of the Ionic Transport Properties within the Argyrodite Li₆PS_{5-x}Se_xI. *ACS Appl. Energy Mater.* **2020**, *3* (1), 9–18.
- (7) Hori, S.; Suzuki, K.; Hirayama, M.; Kato, Y.; Saito, T.; Yonemura, M.; Kanno, R. Synthesis, Structure, and Ionic Conductivity of Solid Solution, Li_{10+δ}M_{1+δ}P_{2-δ}S₁₂ (M = Si, Sn). *Faraday Discuss.* 2014, 176, 83–94.
- (8) Muy, S.; Bachman, J. C.; Giordano, L.; Chang, H.-H.; Abernathy, D. L.; Bansal, D.; Delaire, O.; Hori, S.; Kanno, R.; Maglia, F.; Lupart, S.; Lamp, P.; Shao-Horn, Y. Tuning Mobility and Stability of Lithium Ion Conductors Based on Lattice Dynamics. *Energy Environ. Sci.* 2018, 11 (4), 850–859.
- (9) Kraft, M. A.; Culver, S. P.; Calderon, M.; Böcher, F.; Krauskopf, T.; Senyshyn, A.; Dietrich, C.; Zevalkink, A.; Janek, J.; Zeier, W. G. Influence of Lattice Polarizability on the Ionic Conductivity in the Lithium Superionic Argyrodites Li₆PS₅X (X = Cl, Br, I). *J. Am. Chem. Soc.* **2017**, *139* (31), 10909–10918.
- (10) Murayama, M.; Sonoyama, N.; Yamada, A.; Kanno, R. Material Design of New Lithium Ionic Conductor, Thio-LISICON, in the Li₂S-P₂S₅ System. *Solid State Ionics* **2004**, *170* (3–4), 173–180.
- (11) Homma, K.; Yamamoto, T.; Watanabe, S.; Tanaka, T. Enlarged Lithium-Ions Migration Pathway by Substitution of B³⁺ for P⁵⁺ in Li₃PS₄. *ECS Trans*. **2013**, *50* (26), 307–314.
- (12) Liang, J.; Li, X.; Wang, S.; Adair, K. R.; Li, W.; Zhao, Y.; Wang, C.; Hu, Y.; Zhang, L.; Zhao, S.; Lu, S.; Huang, H.; Li, R.; Mo, Y.; Sun, X. Site-Occupation-Tuned Superionic

- Li_xScCl_{3+x} Halide Solid Electrolytes for All-Solid-State Batteries. *J. Am. Chem. Soc.* **2020**, *142* (15), 7012–7022.
- (13) Sakuda, A.; Hayashi, A.; Tatsumisago, M. Sulfide Solid Electrolyte with Favorable Mechanical Property for All-Solid-State Lithium Battery. *Sci. Rep.* **2013**, *3*, 2–6.
- (14) Kanno, R.; Murayama, M. Lithium Ionic Conductor Thio-LISICON: The Li₂S-GeS₂-P₂S₅ System. *J. Electrochem. Soc.* **2001**, *148* (7), 742–746.
- (15) Kamaya, N.; Homma, K.; Yamakawa, Y.; Hirayama, M.; Kanno, R.; Yonemura, M.; Kamiyama, T.; Kato, Y.; Hama, S.; Kawamoto, K.; Mitsui, A. A Lithium Superionic Conductor. *Nat. Mater.* **2011**, *10* (9), 682–686.
- (16) Schlem, R.; Muy, S.; Prinz, N.; Banik, A.; Shao-Horn, Y.; Zobel, M.; Zeier, W. G. Mechanochemical Synthesis: A Tool to Tune Cation Site Disorder and Ionic Transport Properties of Li₃MCl₆ (M = Y, Er) Superionic Conductors. *Adv. Energy Mater.* 2020, 10 (6), 1903719.
- (17) Zhou, L.; Kwok, C. Y.; Shyamsunder, A.; Zhang, Q.; Wu, X.; Nazar, L. F. A New Halospinel Superionic Conductor for High-Voltage All Solid State Lithium Batteries. *Energy Environ. Sci.* **2020**, *13* (7), 2056–2063.
- (18) Li, X.; Liang, J.; Chen, N.; Luo, J.; Adair, K. R.; Wang, C.; Banis, M. N.; Sham, T.; Zhang, L.; Zhao, S.; Lu, S.; Huang, H.; Li, R.; Sun, X. Water-Mediated Synthesis of a Superionic Halide Solid Electrolyte. *Angew. Chemie* **2019**, *131* (46), 16579–16584.
- (19) Deiseroth, H.-J.; Kong, S.-T.; Eckert, H.; Vannahme, J.; Reiner, C.; Zaiß, T.; Schlosser, M. Li₆PS₅X: A Class of Crystalline Li-Rich Solids With an Unusually High Li⁺ Mobility. *Angew. Chemie* **2008**, *120* (4), 767–770.
- (20) Adeli, P.; Bazak, J. D.; Huq, A.; Goward, G. R.; Nazar, L. F. Influence of Aliovalent

- Cation Substitution and Mechanical Compression on Li-Ion Conductivity and Diffusivity in Argyrodite Solid Electrolytes. *Chem. Mater.* **2021**, *33* (1), 146–157.
- (21) Zhou, L.; Minafra, N.; Zeier, W. G.; Nazar, L. F. Innovative Approaches to Li-Argyrodite Solid Electrolytes for All-Solid-State Lithium Batteries. *Acc. Chem. Res.* **2021**, *54* (12), 2717–2728.
- (22) Bron, P.; Johansson, S.; Klaus, Z.; Schmedt auf der Günne, J.; Dehnen, S.; Roling, B. Li₁₀SnP₂S₁₂: An Affordable Lithium Superionic Conductor. *J. Am. Chem. Soc.* **2013**, *135* (42), 15694–15697.
- (23) Kato, Y.; Saito, R.; Sakano, M.; Mitsui, A.; Hirayama, M.; Kanno, R. Synthesis, Structure and Lithium Ionic Conductivity of Solid Solutions of Li₁₀(Ge_{1-x}M_x)P₂S₁₂ (M = Si, Sn). *J. Power Sources* **2014**, *271*, 60–64.
- (24) Krauskopf, T.; Culver, S. P.; Zeier, W. G. Bottleneck of Diffusion and Inductive Effects in Li₁₀Ge_{1-x}Sn_xP₂S₁₂. *Chem. Mater.* **2018**, *30* (5), 1791–1798.
- (25) Culver, S. P.; Squires, A. G.; Minafra, N.; Armstrong, C. W. F.; Krauskopf, T.; Böcher, F.; Li, C.; Morgan, B. J.; Zeier, W. G. Evidence for a Solid-Electrolyte Inductive Effect in the Superionic Conductor Li₁₀Ge_{1-x}Sn_xP₂S₁₂. J. Am. Chem. Soc. 2020, 142 (50), 21210–21219.
- (26) Kanno, R.; Hata, T.; Kawamoto, Y.; Irie, M. Synthesis of a New Lithium Ionic Conductor, Thio-LISICON-Lithium Germanium Sulfide System. *Solid State Ionics* **2000**, *130* (1), 97–104.
- Minafra, N.; Hogrefe, K.; Barbon, F.; Helm, B.; Li, C.; Wilkening, H. M. R.; Zeier, W.
 G. Two-Dimensional Substitution: Toward a Better Understanding of the Structure–
 Transport Correlations in the Li-Superionic Thio-LISICONs. *Chem. Mater.* 2021, 33 (2), 727–740.

- (28) Murayama, M.; Kanno, R.; Kawamoto, Y.; Kamiyama, T. Structure of the Thio-LISICON, Li4GeS4. *Solid State Ionics* **2002**, *155*, 789–794.
- (29) Matsushita, Y.; Kanatzidis, M. G. Synthesis and Structure of Li₄GeS₄. *Zeitschrift fur Naturforsch. B* **1998**, *53*, 23–30.
- (30) Ohno, S.; Banik, A.; Dewald, G. F.; Kraft, M. A.; Krauskopf, T.; Minafra, N.; Till, P.; Weiss, M.; Zeier, W. G. Materials Design of Ionic Conductors for Solid State Batteries. *Prog. Energy* **2020**, *2* (2), 022001.
- (31) Murayama, M.; Kanno, R.; Irie, M.; Ito, S.; Hata, T.; Sonoyama, N.; Kawamoto, Y. Synthesis of New Lithium Ionic Conductor Thio-LISICON Lithium Silicon Sulfides System. *J. Solid State Chem.* **2002**, *168* (1), 140–148.
- (32) Kwak, H.; Park, K. H.; Han, D.; Nam, K. W.; Kim, H.; Jung, Y. S. Li⁺ Conduction in Air-Stable Sb-Substituted Li₄SnS₄ for All-Solid-State Li-Ion Batteries. *J. Power Sources* **2020**, *446*, 227338.
- (33) Zhang, Z.; Zhang, J.; Sun, Y.; Jia, H.; Peng, L.; Zhang, Y.; Xie, J. Li_{4-x}Sb_xSn_{1-x}S₄ Solid Solutions for Air-Stable Solid Electrolytes. *J. Energy Chem.* **2020**, *41*, 171–176.
- (34) Sahu, G.; Lin, Z.; Li, J.; Liu, Z.; Dudney, N.; Liang, C. Air-Stable, High-Conduction Solid Electrolytes of Arsenic-Substituted Li₄SnS₄. *Energy Environ. Sci.* **2014**, *7* (3), 1053–1058.
- (35) Sahu, G.; Rangasamy, E.; Li, J.; Chen, Y.; An, K.; Dudney, N.; Liang, C. A High-Conduction Ge Substituted Li₃AsS₄ Solid Electrolyte with Exceptional Low Activation Energy. *J. Mater. Chem. A* **2014**, *2* (27), 10396–10403.
- (36) Shannon, R. D. Revised Effective Ionic Radii and Systematic Studies of Interatomic Distances in Halides and Chalcogenides. *Acta Crystallogr. Sect. A* **1976**, *32* (5), 751–

- (37) Till, P.; Agne, M. T.; Kraft, M. A.; Courty, M.; Famprikis, T.; Ghidiu, M.; Krauskopf, T.; Masquelier, C.; Zeier, W. G. Two-Dimensional Substitution Series Na₃P_{1-x}Sb_xPS_{4-y}Se_y Beyond Static Description of Structural Bottlenecks for Na⁺ Transport. *Chem. Mater.* 2022, 34 (5), 2410–2421.
- (38) Coelho, A. A. TOPAS-Academic 2007, Brisbane.
- (39) Huq, A.; Kirkham, M.; Peterson, P. F.; Hodges, J. P.; Whitfield, P. S.; Page, K.; Hügle, T.; Iverson, E. B.; Parizzi, A.; Rennich, G. POWGEN: Rebuild of a Third-Generation Powder Diffractometer at the Spallation Neutron Source. *J. Appl. Crystallogr.* 2019, 52 (5), 1189–1201.
- (40) Momma, K.; Izumi, F. VESTA 3 for Three-Dimensional Visualization of Crystal, Volumetric and Morphology Data. *J. Appl. Crystallogr.* **2011**, *44* (6), 1272–1276.
- (41) Zhang, W.; Weber, D. A.; Weigand, H.; Arlt, T.; Manke, I.; Schröder, D.; Koerver, R.; Leichtweiss, T.; Hartmann, P.; Zeier, W. G.; Janek, J. Interfacial Processes and Influence of Composite Cathode Microstructure Controlling the Performance of All-Solid-State Lithium Batteries. ACS Appl. Mater. Interfaces 2017, 9 (21), 17835–17845.
- (42) Brug, G. J.; van den Eeden, A. L. G.; Sluyters-Rehbach, M.; Sluyters, J. H. The Analysis of Electrode Impedances Complicated by the Presence of a Constant Phase Element. *J. Electroanal. Chem. Interfacial Electrochem.* **1984**, *176* (1–2), 275–295.
- (43) Chen, H.; Wong, L. L.; Adams, S. SoftBV a Software Tool for Screening the Materials Genome of Inorganic Fast Ion Conductors. *Acta Crystallogr. Sect. B Struct. Sci. Cryst. Eng. Mater.* **2019**, 75 (1), 18–33.
- (44) Adams, S. Bond Valence Analysis of Structure-Property Relationships in Solid

- Electrolytes. J. Power Sources 2006, 159 (1), 200–204.
- (45) Prasada Rao, R.; Chen, H.; Adams, S. Stable Lithium Ion Conducting Thiophosphate Solid Electrolytes Li_x(PS₄)_yX_z (X = Cl, Br, I). *Chem. Mater.* **2019**, *31* (21), 8649–8662.
- (46) Adams, S.; Rao, R. P. Transport Pathways for Mobile Ions in Disordered Solids from the Analysis of Energy-Scaled Bond-Valence Mismatch Landscapes. *Phys. Chem. Chem. Phys.* **2009**, *11* (17), 3210.
- (47) Chen, H.; Adams, S. Bond Softness Sensitive Bond-Valence Parameters for Crystal Structure Plausibility Tests. *IUCrJ* **2017**, *4*, 614–625.
- (48) Takata, M.; Nishibori, E.; Sakata, M. Charge Density Studies Utilizing Powder Diffraction and MEM. Exploring of High Tc Superconductors, C 60 Superconductors and Manganites. *Zeitschrift für Krist. Cryst. Mater.* **2001**, *216* (2), 71–86.
- (49) Momma, K.; Ikeda, T.; Belik, A. A.; Izumi, F. Dysnomia, a Computer Program for Maximum-Entropy Method (MEM) Analysis and Its Performance in the MEM-Based Pattern Fitting. *Powder Diffr.* **2013**, *28* (3), 184–193.
- (50) Kuhn, A.; Narayanan, S.; Spencer, L.; Goward, G.; Thangadurai, V.; Wilkening, M. Li Self-Diffusion in Garnet-Type Li₇La₃Zr₂O₁₂ as Probed Directly by Diffusion-Induced ⁷Li Spin-Lattice Relaxation NMR Spectroscopy. *Phys. Rev. B* **2011**, *83* (9), 094302.
- (51) Hodge, I. M.; Ingram, M. D.; West, A. R. Impedance and Modulus Spectroscopy of Polycrystalline Solid Electrolytes. *J. Electroanal. Chem.* **1976**, *74* (2), 125–143.
- (52) Kimura, T.; Kato, A.; Hotehama, C.; Sakuda, A.; Hayashi, A.; Tatsumisago, M. Preparation and Characterization of Lithium Ion Conductive Li₃SbS₄ Glass and Glass-Ceramic Electrolytes. *Solid State Ionics* **2019**, *333*, 45–49.
- (53) Böhmer, R.; Jeffrey, K. R.; Vogel, M. Solid-State Li NMR with Applications to the

- Translational Dynamics in Ion Conductors. *Prog. Nucl. Magn. Reson. Spectrosc.* **2007**, 50, 87–174.
- (54) Wilkening, M.; Epp, V.; Feldhoff, A.; Heitjans, P. Tuning the Li Diffusivity of Poor Ionic Conductors by Mechanical Treatment: High Li Conductivity of Strongly Defective LiTaO₃ Nanoparticles. J. Phys. Chem. C 2008, 112, 9291–9300.
- (55) Hendrickson, J. R.; Bray, P. J. A Phenomenological Equation for NMR Motional Narrowing in Solids. *J. Magn. Reson.* **1973**, *9*, 341–357.
- (56) Hogrefe, K.; Minafra, N.; Zeier, W. G.; Wilkening, H. M. R. Tracking Ions the Direct Way: Long-Range Li⁺ Dynamics in the Thio- LISICON Family Li₄MCh₄ (M = Sn, Ge; Ch = S, Se) as Probed by ⁷Li NMR Relaxometry and ⁷Li Spin-Alignment Echo NMR. *J. Phys. Chem. C* **2021**, *125*, 2306–2317.
- (57) Wilkening, M.; Heitjans, P. From Micro to Macro: Access to Long-Range Li⁺ Diffusion Parameters in Solids via Microscopic ^{6,7}Li Spin-Alignment Echo NMR Spectroscopy. *ChemPhysChem* **2012**, *13*, 53–65.
- (58) Arbi, K.; Lazarraga, M. G.; Ben Hassen Chehimi, D.; Ayadi-Trabelsi, M.; Rojo, J. M.; Sanz, J. Lithium Mobility in Li_{1.2}Ti_{1.8}R_{0.2}(PO₄)₃ Compounds (R = Al, Ga, Sc, In) as Followed by NMR and Impedance Spectroscopy. *Chem. Mater.* **2004**, *16* (2), 255–262.
- (59) Bloembergen, N.; Purcell, E. M.; Pound, R. V. Relaxation Effects in Nuclear Magnetic Resonance Absorption. *Phys. Rev.* **1948**, *73* (7), 679–712.
- (60) Cussen, E. J. The Structure of Lithium Garnets: Cation Disorder and Clustering in a New Family of Fast Li⁺ Conductors. *Chem. Commun.* **2006**, 412–413.
- (61) Nishino, S.; Fujiwara, T.; Yamasaki, H. Nanosecond Quantum Molecular Dynamics Simulations of the Lithium Superionic Conductor. *Phys. Rev. B* **2014**, *90*, 024303.

- (62) Dippo, O. F.; Vecchio, K. S. A Universal Configurational Entropy Metric for High-Entropy Materials. *Scr. Mater.* **2021**, *201*, 113974.
- (63) Miracle, D. B.; Senkov, O. N. Acta Materialia A Critical Review of High Entropy Alloys and Related Concepts. *Acta Mater.* **2017**, *122*, 448–511.
- (64) Phani Dathar, G. K.; Balachandran, J.; Kent, P. R. C.; Rondinone, A. J.; Ganesh, P. Li-Ion Site Disorder Driven Superionic Conductivity in Solid Electrolytes: A First-Principles Investigation of β-Li₃PS₄. J. Mater. Chem. A 2017, 5 (3), 1153–1159.
- (65) Saha, S.; Rousse, G.; Alcover, I. B.; Courty, M.; Corte, D. A. D.; Tarascon, J.-M. Polymorphism in Li₄Zn(PO₄)₂ and Stabilization of Its Structural Disorder to Improve Ionic Conductivity. *Chem. Mater.* **2018**, *30*, 1379–1390.
- (66) Zhou, L.; Assoud, A.; Shyamsunder, A.; Huq, A.; Zhang, Q.; Hartmann, P.; Kulisch, J.;
 Nazar, L. F. An Entropically Stabilized Fast-Ion Conductor: Li_{3.25}[Si_{0.25}P_{0.75}]S₄. Chem.
 Mater. 2019, 31 (19), 7801–7811.
- (67) Schlem, R.; Bernges, T.; Li, C.; Kraft, M. A.; Minafra, N.; Zeier, W. G. Lattice Dynamical Approach for Finding the Lithium Superionic Conductor Li₃ErI₆. *ACS Appl. Energy Mater.* **2020**, *3* (4), 3684–3691.
- (68) Schlem, R.; Banik, A.; Ohno, S.; Suard, E.; Zeier, W. G. Insights into the Lithium Sub-Structure of Superionic Conductors Li₃YCl₆ and Li₃YBr₆. *Chem. Mater.* **2021**, *33* (1), 327–337.
- (69) Gautam, A.; Sadowski, M.; Prinz, N.; Eickhoff, H.; Minafra, N.; Ghidiu, M.; Culver, S.; Albe, K.; Fässler, T.; Zobel, M.; Zeier, W. Rapid Crystallization and Kinetic Freezing of Site-Disorder in the Lithium Superionic Argyrodite Li₆PS₅Br. *Chem. Mater.* **2019**, *31*, 10178–10185.

- (70) Gautam, A.; Sadowski, M.; Ghidiu, M.; Minafra, N.; Senyshyn, A.; Albe, K.; Zeier, W.
 G. Engineering the Site-Disorder and Lithium Distribution in the Lithium Superionic
 Argyrodite Li₆PS₅Br. *Chem. Mater.* 2019, 31, 10178–10185.
- (71) Leube, B. T.; Inglis, K. K.; Carrington, E. J.; Sharp, P. M.; Shin, J. F.; Neale, A. R.; Manning, T. D.; Pitcher, M. J.; Hardwick, L. J.; Dyer, M. S.; Blanc, F.; Claridge, J. B.; Rosseinsky, M. J. Lithium Transport in Li_{4.4}M_{0.4}M'_{0.6}S₄ (M = Al³⁺, Ga³⁺, and M' = Ge⁴⁺, Sn⁴⁺): Combined Crystallographic, Conductivity, Solid State NMR, and Computational Studies. *Chem. Mater.* **2018**, *30* (20), 7183–7200.
- (72) Morgan, B. J. Mechanistic Origin of Superionic Lithium Diffusion in Anion-Disordered Li₆PS₅X Argyrodites. *Chem. Mater.* **2021**, *33*, 2004–2018.

TOC

